Weyl nodes and magnetostructural instability in antiperovskite Mn3ZnC

Weyl nodes and magnetostructural instability in antiperovskite Mn_3ZnC

Cite as: APL Mater. 7, 121104 (2019); doi: 10.1063/1.5129689
Submitted: 30 September 2019 • Accepted: 25 November 2019 •
Published Online: 12 December 2019

S. M. L. Teicher,[1,a)] I. K. Svenningsson,[2,3] L. M. Schoop,[4] and R. Seshadri[1]

AFFILIATIONS

[1]Materials Department and Materials Research Laboratory, University of California, Santa Barbara, California 93106, USA
[2]Materials Research Laboratory, University of California, Santa Barbara, California 93106, USA
[3]Department of Applied Physics, Chalmers University of Technology, Göteborg 412 96, Sweden
[4]Department of Chemistry, Princeton University, Princeton, New Jersey 08540, USA

Note: This paper is part of the Special Topic on Topological Semimetals–New Directions.
[a)]**Electronic mail:** steicher@ucsb.edu

ABSTRACT

The room temperature ferromagnetic phase of the cubic antiperovskite Mn_3ZnC is suggested from first-principles calculation to be a nodal line Weyl semimetal. Features in the electronic structure that are the hallmark of a nodal line Weyl state—a large density of linear band crossings near the Fermi level—can also be interpreted as signatures of a structural and/or magnetic instability. Indeed, it is known that Mn_3ZnC undergoes transitions upon cooling from a paramagnetic to a cubic ferromagnetic state under ambient conditions and then further into a noncollinear ferrimagnetic tetragonal phase at a temperature between 250 K and 200 K. The existence of Weyl nodes and their destruction via structural and magnetic ordering are likely to be relevant to a range of magnetostructurally coupled materials.

I. INTRODUCTION

Antiperovskite carbides are a family of materials with the cubic perovskite structure and formula X_3BC where X is the least electronegative element in the formula and C is carbon (see Fig. 1). Related carbides have a long history in metallurgical research, associated with the larger family of so-called *MAX* phases.[1] Several members of the family such as Co_3AlC[2] have been explored for applications in structural alloys and Mn_3SnC[3] and carbon-doped Mn_3ZnN[4] exhibit negative thermal expansion effects. Some antiperovskite carbides are also of interest for their functionality. Mn_3GaC is known to display giant magnetoresistance[5] and Ni_3MgC is an 8 K superconductor, the latter rationalized by first principles calculations as being associated with a flat band (FB) with large density of states (DOS) near the Fermi level.[6,7]

More recently, the larger class of antiperovskites has been explored due to the prediction of topological electronic states. The Ca_3PbO and Ca_3BiN families include Dirac semimetals[8,9]—materials with a graphene-like linear-band crossing, or Dirac cone, near the Fermi level[10,11]—as well as topological insulators[12] and topological crystalline insulators[13] with a bulk band gap and metallic surface states. Magnetization and resistivity data in two recent studies on Sr_3PbO and Sr_3SnO provide preliminary evidence for Dirac transport[14] and low-temperature superconductivity,[15] respectively. The Cu_3PdN family is predicted to include nodal line semimetals, in which Dirac crossings persist over an extended region, a line, rather than a single point in the Brillouin zone.[16] Nodal line semimetals can host a unique class of drum-head topological surface states with k-vectors connecting all the Dirac nodes on the nodal ring in the Brillouin zone.[17] However, as is common in predicted nodal line compounds, the relatively large spin-orbit coupling (SOC) due to the heavy Pd atom in Cu_3PdN partially gaps the nodal line, preventing the realization of a true nodal line semimetal.[16]

The topic of this letter is Mn_3ZnC, a material that has been explored since the 1950s due to its interesting magnetic transitions. In a series of studies, Butters and Myers,[18] Brockhouse and Myers,[19] and Swanson and Friedberg[20] provided early characterization of these transitions, which include a paramagnetic (PM) to ferromagnetic (FM) transition with reported Curie temperatures 350 K < T_C < 500 K[18,21,22] and antiferromagnetic ordering with reported Néel

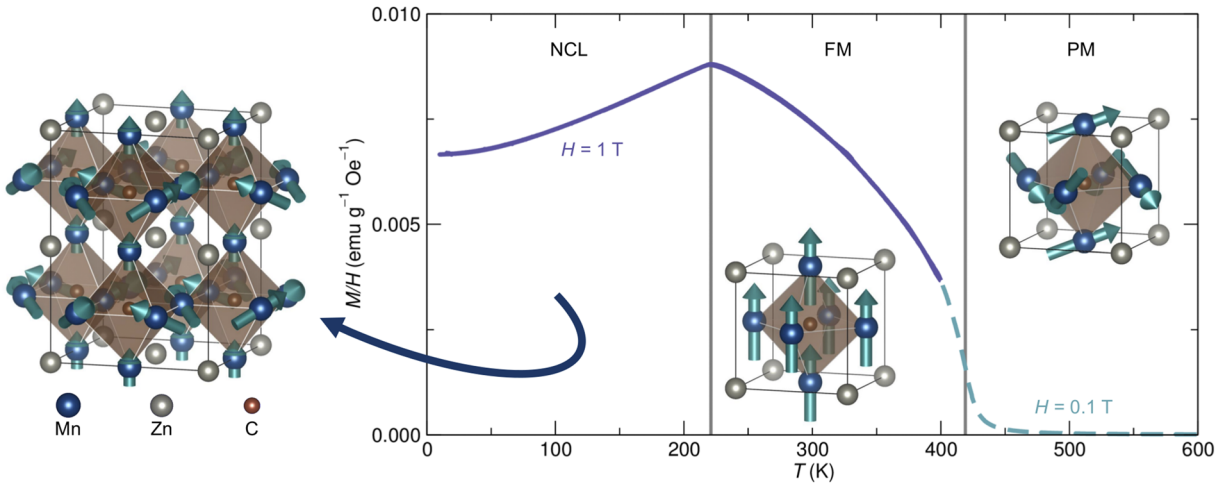

FIG. 1. Reported crystal and magnetic structures of Mn_3ZnC. Mn_3ZnC undergoes transitions from paramagnetic (PM) to ferromagnetic (FM) states in the cubic antiperovskite structure with $T_C \approx 420$ K. A lower temperature antiferromagnetic transition with $T_N \approx 219$ K is associated with noncollinear ferrimagnetic ordering in a tetragonal structure.

temperatures 215 K < T_N < 233 K.[18,21,22] In the 1970s, Fruchart and colleagues solved the magnetic structures via neutron diffraction, determining the [001] ferromagnetic room temperature structure and more complex noncollinear low temperature structure shown in Fig. 1.[21,23] The magnetic moments, localized on the Mn site, are approximately 1.3 μ_B in the ferromagnetic state and 2.7 μ_B and 1.6 μ_B in the noncollinear, antiferromagnetically coupled and collinear, ferromagnetically aligned layers of the low temperature structure, respectively. The low magnetic moments suggest that the magnetism is fairly itinerant in this system relative to most Mn magnetic materials. In the 1980s, the transition shifts in Mn_3ZnC were studied under large applied magnetic fields and pressures.[22,24]

Theoretical attempts to explain the magnetic transitions in Mn_3ZnC have focused on the presence of a large Fermi level flat band. In 1975, Jardin and Labbé proposed that the main bonding interactions in this system originate from Mn d_{xz}, d_{yz}, and C p orbitals and generated a tight-bonding model with sharp peaks in the density of states.[25] Should the Fermi level lie at one of these peaks, the ferromagnetic to paramagnetic transition could be explained by Stoner exchange and the low temperature structural distortion by a Jahn-Teller-like energetic benefit accrued through further reducing the density of states near the Fermi level. Non-spin polarized density of states calculations reported later indeed found a large spike in the density of states just above the calculated Fermi level.[26] This work was extended with density of states calculations on both the spin-polarized, ferromagnetic and noncollinear, ferrimagnetic structures, demonstrating that spin polarization opens up a pseudogap at the Fermi-level in the ferromagnetic phase, consistent with a Stoner exchange mechanism, and that a wider gap opens just below E_F in the ferrimagnetic state.[27]

Here, we use first principles calculations to show that the cubic ferromagnetic phase of Mn_3ZnC that is stable at room temperature is a nodal line Weyl semimetal. Although Weyl nodes are common in ferromagnetic metals, including bcc Fe,[28] to-date studies on Weyl nodal lines are more of a rarity: the first experimental work toward verification of a Weyl nodal line has recently been completed for the Heusler compound $MnCo_2Ga$.[29] In Mn_3ZnC, we present a computational bonding analysis that provides qualitative explanations for the magnetic transitions that create and destroy this delicate Weyl ferromagnet phase. Motivated by interest in the Weyl nodes and their potential role in magnetostructural instabilities, we experimentally revisit the transitions in this material via magnetoentropic mapping, which is a sensitive probe for low energy and metamagnetic reordering.

II. METHODS

A. Computational

Density functional theory simulations were completed in VASP[30–32] and WIEN2k[33] using the Perdew, Burke, Ernzerhof functional[34] with projector-augmented waves[35,36] and linear augmented plane waves + local orbitals,[37] respectively. PAW potentials for VASP were selected based on version 5.2 recommendations. All calculations described in the text were performed in VASP except for the band irrep assignments of Fig. 3(c), which were completed using the IRREP subprogram of WIEN2k. A 17 × 17 × 17 Γ-centered k-mesh was employed for electronic structure simulations of the ferromagnetic phase. These calculations are well-converged for much lower density k-meshes, but high k-mesh density is desirable for accurate Wannier function fitting; an 8 × 8 × 8 mesh was used for relaxation steps. Calculations for the expanded low temperature tetragonal cell were performed using a 5 × 5 × 4 Γ-centered k-mesh for relaxation and self-consistent steps and a 7 × 7 × 5 mesh for the density of states. The plane wave energy cutoff for VASP and the plane-wave expansion parameter, RKMAX, for WIEN2k were set to values better than 500 eV and 8.0, respectively. Tetrahedral smearing with Blöchl corrections[38] was used for relaxations and self-consistent calculations. Structures were relaxed in VASP via the conjugate gradient descent algorithm with an energy

convergence cutoff of 10^{-4} eV. Subsequent self-consistent static calculations and non-self-consistent electronic structure calculations were performed using VASP and WIEN2k with energy convergence better than 10^{-5} eV. The surface states of Mn_3ZnC were determined by projecting our VASP calculations onto maximally localized Wannier functions using Wannier90,[39] starting from initial projectors corresponding to valence orbitals (Mn d; Zn s, p, d; C p; with a frozen fitting window $E_F \pm 2$ eV), constructing a tight-binding model from these localized Wannier functions, and finally using the Wannier Tools package[40] to calculate the Green's function spectrum.[41] The VASP simulations input into Wannier90 were performed with noncollinear spins on a nonsymmetrized k-mesh with and without SOC. The Mn magnetic moments in these simulations were constrained to point along [001]. Fine k-mesh mapping of the Weyl node locations in the 3D Brillouin zone was also performed on this tight-binding model. Berry curvature was determined using the Wannier90 KSLICE module. The band structure of Fig. 5 was unfolded using BandUP.[42,43] Orbital projections, density of states, and crystal orbital Hamiltonian populations (COHPs) for the high temperature phase were determined using LOBSTER.[44–47] The density of states and orbital projections for the low temperature structure are reported using default VASP projections as LOBSTER does not support noncollinear magnetism. A postprocess Gaussian smoothing with standard deviation 0.2 eV was applied to all calculated density of states and COHPs. Structures are visualized with VESTA.[48]

B. Experimental

Samples of Mn_3ZnC were produced by a two-step solid-state synthesis, following a previous report,[22] starting from stoichiometric quantities of Mn (Fisher Scientific, 99.95%), Zn (Strem Chemicals, 99.9%), and C (Alfa Aesar, 99%) and adding 7 Mass % Zn during the second mixing step. Additional Zn was included to decrease the Mn:Zn ratio of the final material toward 3. Wavelength-dispersive X-ray fluorescence measurements performed on a Rigaku ZSX Primus IV suggest that the composition is close to $Mn_{3.16}Zn_{0.84}C$. Magnetic measurements were performed on a Quantum Design MPMS3 operating under vibrating sample magnetometer mode. High temperature measurements ($T > 400$ K) including the PM-FM transition utilized the oven heater stick attachment option while lower temperature measurements used a standard brass sample holder. The magnetization curve in Fig. 1 was generated by measuring magnetization at fields of 1 T, 0.1 T, below and above 300 K, respectively, and normalizing the high temperature magnetization curve such that there was no discontinuity at 300 K. $\partial M/\partial T$ and ΔS_M curves are calculated using methods reported previously.[49] Additional experimental details, including our attempts to develop an original microwave synthesis route for this and related antiperovskite carbides, are provided in the supplementary material.

III. RESULTS

We first consider the density of states (DOS) for the cubic, ferromagnetic phase of Mn_3ZnC, as shown in Fig. 2. We consider only Mn d states because other orbital contributions are small near the Fermi level (see the supplementary material). From Fig. 2(a), we can see that the DOS is relatively large at the Fermi level and

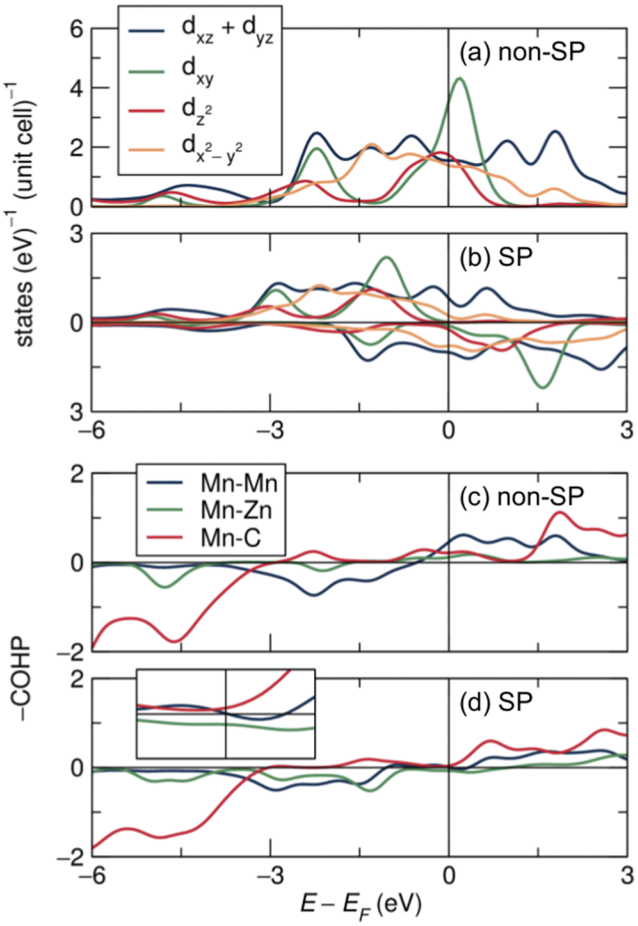

FIG. 2. Density of states and crystal orbital Hamiltonian population for the ferromagnetic phase. Partial density of states of the dominant Mn d-orbital contributions are compared (a) without and (b) with spin polarization. The crystal orbital Hamiltonian populations for Mn-Mn, Mn-Zn, and Mn-C bonding are presented (c) without and (d) with spin polarization. Inset of (d) shows close-up of COHP in the region just about the Fermi level ($E_F \pm 0.5$ eV).

that there is a large DOS peak just above this level. This is consistent with the hypothesized Stoner exchange mechanism for the ferromagnetism in this material. Indeed, in the spin-polarized calculation, Fig. 2(b), we find that the onset of ferromagnetism eliminates this DOS peak, reducing the Fermi-level DOS. The mechanism appears to be somewhat distinct from that originally proposed by Jardin and Labbé, however, as the near-Fermi level DOS peak in the non-spin-polarized calculation originates from Mn d_{xy} states, rather than d_{xz}/d_{yz} states. Here, we consider the local symmetry of the Mn d orbitals in terms of the cell coordinates (this is the preference in prior literature). From this perspective, we find that the d_{xz}/d_{yz} orbitals are equivalent and point from one Mn toward its Mn neighbors and are involved in strong Mn-Mn bonding and some Mn-C bonding. d_{z^2} and d_{xy} orbitals have lobes pointing from Mn toward C and Zn atoms and are expected to be important in Mn-C and Mn-Zn bonding, respectively. Finally, $d_{x^2-y^2}$ orbitals point directly

toward no other atom and are expected to be more weakly involved in bonding.

The proposed picture of a simple ferromagnetic distortion is further complicated when we consider these bonding interactions via the crystal orbital Hamiltonian population (COHP), a quantity derived from wave function overlap that is negative for bonding and positive for antibonding interactions. In a normal ferromagnet, such as iron, the COHP shows significant antibonding at the Fermi level.[50] By splitting the spin populations, the normal ferromagnet is able to stabilize and fill a greater number of bonding states near the Fermi level, and relatively few antibonding states. The d_{xy} orbitals, however, are not expected to be strongly (anti)bonding; the COHP, Fig. 2(c), confirms the relatively weak strength of Mn-Zn interactions in this energy region. Rather than elimination of a sharp antibonding peak due to the d_{xy} states, the spin-polarization appears to be stabilized by two effects: first, the reduction of the antibonding states just below the Fermi level and, second, the development of Mn-Zn bonding states originating from the originally weakly bonding d_{xy} band, Fig. 2(d). In the end, rather than a magnetic metal with a large number of bonding states at the Fermi level, we are left with a semimetal that has nonbonding character near E_F. Examining the COHP immediately about the Fermi level [Fig. 2(d), inset], we find that the Mn-Zn interactions are bonding and the Mn-C interactions are antibonding. The Mn-Mn COHP displays a subtle cross-over from antibonding to bonding at the Fermi level. Such a Fermi level COHP crossover is typical of antiferromagnetic metals, although it usually involves bonding states below the Fermi level and antibonding states immediately above. In analog to the simple tight-binding chain model of 1*s* orbitals, which forms a metal with a completely filled bonding band that can support a symmetry breaking lattice displacement of the atoms with a resulting bandgap, the Peierls distortion,[51] the bonding in Mn_3ZnC appears susceptible to symmetry breaking via both physical lattice distortion and antiferromagnetic ordering, either of which could distinguish the Mn sites and generate an electronic gap.

This ferromagnetic semimetal phase becomes much more interesting when we consider the electronic band structure in Fig. 3, which reveals several Weyl nodes. Figure 3(a) depicts the bulk cubic Brillouin zone. Figure 3(b) presents the spin-polarized band structure with orange majority bands and blue minority bands. Five features of interest are labeled. First, despite the gapping of the density of states at the Fermi level, a flat band, FB, persists along Γ-*X* right at the Fermi level. Along *X*-*M* and *M*-Γ, we find linear band crossings, Weyl nodes, in the minority bands, labeled W_1 and W_2. On either

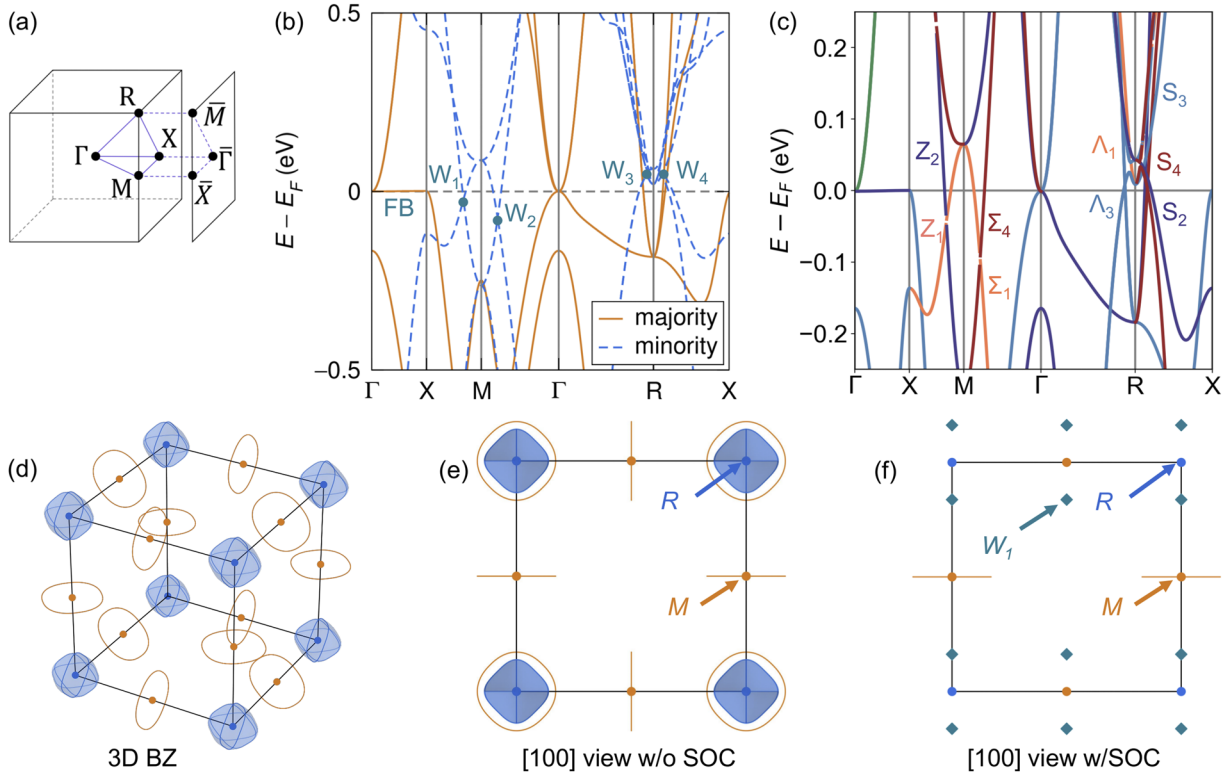

FIG. 3. Bulk band structure and Weyl crossings. (a) High-symmetry points in the bulk Brillouin zone and (100)/(001) surface-projected Brillouin zone. (b) Spin-polarized band structure showing a flat-band in the majority states and four types of near-Fermi level Weyl crossing. (c) Close-up band structure with bands colored by irreducible representation. [(d)–(f)] Schematics of Weyl surfaces in the 3D Brillouin zone. (d) 3D view without SOC. (e) (100) view without SOC. (f) (100) view with SOC. In the absence of SOC, nodal loops are displayed around *M* (orange) and 3D nodal surfaces around *R* (blue). With magnetization along [001], SOC gaps the nodal surfaces and many of the nodal loops, leaving behind $k_z = 0$ nodal loops and isolated W_1 nodes.

side of the R point, we also find linear band crossings just above the Fermi level involving both the majority and minority bands. The Weyl nodes on either side of R are labeled W_3 and W_4. Note, however, that there are actually several Weyl nodes on either side of R, and this labeling is a reduction for the sake of simplicity.

The colors of the bands in Fig. 3(c) depict the irreducible representations (irreps) of bands involved in the Weyl crossings. A band crossing is protected against gapping if the irreps of the two crossing bands are different; this represents orthogonality of the electronic states generating these bands. In the absence of spin-orbit coupling (SOC), we can consider this system in the paramagnetic space group ($Pm\bar{3}m$, No. 221). The point group of the k-vectors along X-M, M-Γ, and R-X is C_{2v} and along Γ-R the point group is C_{3v}. The Z_1 and Z_2 irreps differ in their symmetry with respect to C_2 rotation and the mirror operation σ_v', indicating that the W_1 node is protected by these operations. The Σ_1 and Σ_4 irreps differ with respect to C_2 rotation and the mirror operation σ_v. The W_4 nodes involve crossings of S_2, S_3, S_4 bands. The nearest Weyl crossings to the Fermi level along Γ-R and R-X actually involve bands with the same irrep, Λ_3, and S_4, respectively. However, these crossings have bands of orthogonal spinor character, as can be seen when comparing with Fig. 3(b). When SOC is incorporated in the simulation, we must consider the coupling of the magnetic moment to the lattice as well as majority/minority spin mixing interactions. Spin mixing gaps the lowest energy W_3, W_4 crossings, and the breaking of C_2 and mirror symmetries along R-X gaps the W_4 Weyl nodes. The W_3 Weyl crossings due to Λ_1, Λ_3 crossings, meanwhile, are left untouched by SOC. When considering the $k_x = 0$ Brillouin zone plane, which in the non-SOC calculation had been equivalent, however, both nodes are not preserved. Viewing the W_1 and W_2 nodes, on the $k_x = 0$ plane, we find that two of the four W_1 nodes and all four of the W_2 nodes gap out (see the supplementary material for additional details on the effect of SOC). In all cases, the magnitude of the SOC gaps in this material is relatively small due to its low-mass 3d electrons.

Mapping the Weyl nodes in the 3D Brillouin zone, we find that the Weyl nodes in this system are not isolated points, but instead nodal lines and surfaces as depicted in Figs. 3(d) and 3(e). The W_1 and W_2 nodes are part of a nodal line about the M point whereas the lowest energy W_3 and W_4 nodes form a 3D connected surface about the R point. Because of the large number of $W_{3,4}$ Weyl crossings, additional $W_{3,4}$ nodal surfaces may exist which have not been considered. In general, although individual band crossings and nodal lines can be protected, there are no symmetries that can fully protect a 3D nodal surface in the presence of SOC.[52,53] The nodal surfaces depicted in Figs. 3(d) and 3(e) about R are no exception. Because these surfaces result from the crossing of bands of opposite spinor character, and SOC allows spin-channel mixing, these nodal surfaces gap out, and the nodal surface is no longer realized in the final electronic structure after SOC has been incorporated. We find that some of the M nodal lines, however, are protected. The nodal loops on the $k_z = 0$ plane are protected against gapping, while the nodal loops on the k_x, $k_y = 0$ planes gap, leaving only isolated Weyl crossings on the X-M lines. This results in the spin-orbit-gapped configuration shown in Fig. 3(f).

The protection of the M nodal lines is a direct result of the mirror symmetry in the cubic antiperovskite structure. While we have already shown that a combination of C_2 and mirror symmetries protects the band crossings along the Γ-M and M-X high symmetry lines, recomputing the irreps along a generic path through the loop with point group C_s shows the band crossings to be protected by $\overline{C_2}$, which is equivalent to a mirror. The M nodal lines on the $k_z = 0$ plane are preserved under SOC because the [001]-oriented collinear magnetic moment does not break mirror symmetry on this plane. Likewise, the M nodal lines on the k_x, $k_y = 0$ planes gap because the magnetic moment does break the mirror symmetry on these planes—except at the W_1 nodes where the nodal line is tangent to the $k_z = 0$ plane and perpendicular to the [001]-magnetic moment.

These nodal lines are similar to those described in a theoretical tight-binding model of Ca_3P_2 with imposed spin and previously predicted in alloys of the real material $ZrCo_2Sn$ (also under [001] magnetization).[17,54] Due to the soft ferromagnetism and readily reorientable magnetization in $ZrCo_2Sn$, it was proposed that the effective number of Weyl nodes can be tuned by changing the applied field direction. Mn_3ZnC also appears to be a soft ferromagnet and could exhibit similar tunability.

Now that the existence of a protected $k_z = 0$ nodal loop has been established, we might expect to see drumhead surface states connecting between the nodes of this loop on the (001) surface of the material. Figure 4 characterizes the Weyl nodes and their surface states. Weyl nodes can be described as sources and sinks of a quantity called the Berry curvature or Berry flux, defined as

$$\nabla_{\mathbf{k}} \times \langle u_{\mathbf{k}} | i\partial_{\mathbf{k}} u_{\mathbf{k}} \rangle,$$

where $u_{\mathbf{k}}$ represents the Bloch wave function.[55] Low energy electronic excitations analogous to quantum Hall surface states, Fermi arcs, are topologically protected between Weyl nodes emitting and collecting Berry flux.[56] Figure 4(a) shows the magnitude of the Berry flux in the $k_z = 0$ plane at an energy level near the W_1 nodes, highlighting large Berry flux concentration at the nodes. Figures 4(b) and 4(c) present the Weyl surface states projected on a (001) surface. We can see bright surface bands connecting between two W_1 nodes and between two $W_{3,4}$ nodes. [Note, following Fig. 3(a), that the R-M and X-M lines are projected onto the $\overline{M}$ and $\overline{X}$ points when flattening the cubic Brillouin zone along k_z.] The energy level of the W_2 nodes is overlaid in teal. In Fig. 4(c), we can see a Fermi surface cut taken at the W_2 energy level with W_2 nodes clearly visible along $\overline{\Gamma}$-$\overline{X}$. Fermi arcs emitting from the W_2 points can be seen to connect to W_2 nodes in the neighboring Brillouin zone due to the periodic boundary conditions. The $\overline{M}$-$\overline{X}$-$\overline{M}$ line in Fig. 4(b) corresponds to the edges of the plot in Fig. 4(c). Comparing between Figs. 4(b) and 4(c), we see that the surface states connecting the W_1 nodes are identical to the surface states connecting the W_2 nodes; there is indeed a drumhead surface state connecting W_1, W_2, and the other nodes on the nodal line about the M point.

In general, materials with electronic structure features like those in Fig. 3(b)—degenerate flat bands and near-Fermi level band crossings—and especially semimetals with a large concentration of Weyl crossings like this nodal-loop compound, often distort at low temperatures. The energy-lowering transitions that tend to break such nodes are frequently referenced to the idealized models of Peierls or Jahn-Teller distortions. The well-established experimental fact is that a symmetry-breaking low-temperature distortion does

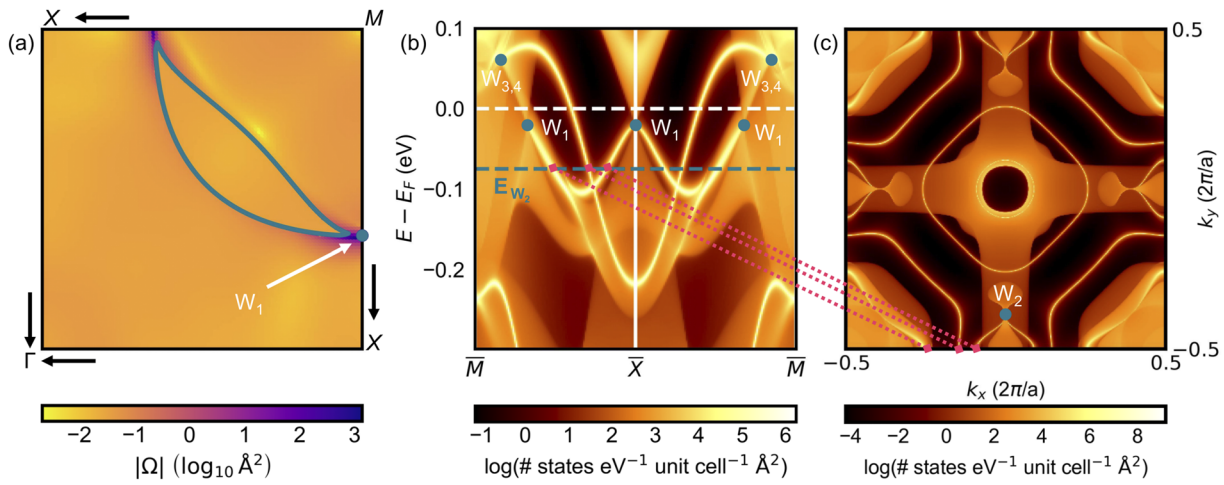

FIG. 4. Characterization of Weyl behavior. (a) $k_z = 0$ cut through the bulk BZ showing large Berry curvature near the W_1 Weyl crossings. A constant energy band-cross-section is overlaid in teal. (b) Surface density of states calculation showing brightly colored surface states connecting between $W_{3,4}$ and between W_1 Weyl points. The energy level of the W_2 Weyl points is also shown. (c) Constant energy Fermi arc calculation for the (001) surface at the energy level of the W_2 nodes. Dotted pink lines connect between surface states at the W_2 level in (b) and the locations of these states in (c) to guide the eye.

activate in this material, involving both a tetragonal stretch of the atomic positions and a magnetic reorientation of the spins with partial antiferromagnetic coupling (Fig. 1).

The density of states of the low temperature structure provides valuable insight for the origin of the low temperature phase. Figure 5 shows the DOS and band structure of the tetragonal low temperature structure with fully noncollinear spins and associated antiferromagnetic coupling. A large pseudogap is seen to

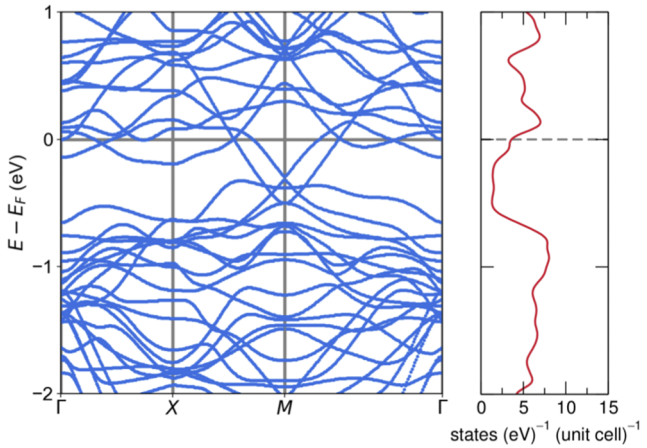

FIG. 5. Band structure and density of states in the noncollinear, low-temperature phase. (Total) DOS values have been normalized to the high-temperature unit cell to provide fair comparison to Fig. 2. A large gap is seen that can be accessed by decreasing the electron count through slight electron deficiency. This unfolded band structure allows a direct comparison of the ferrimagnetic tetragonal cell bands to the band structure of the ferromagnetic cubic unit cell. Although there is significant gapping and removal of Weyl nodes just below the Fermi level, a small number of Weyl nodes persist at E_F.

open up in this case, as would be expected from the description of the antiferromagnetic ordering as a Peierls-like symmetry breaking. We also considered simulations with the tetragonal low temperature structure with no spin polarization and collinear, ferromagnetic polarization. However, because the tetragonal distortion is fairly small, the density of states for these phases exhibit only minor changes with respect to those of Fig. 2. Furthermore, when allowed to relax, the non-spin polarized and collinear spin polarized structures relax into the cubic structure. This analysis suggests that though both are coupled, it is probably the new magnetic ordering, rather than tetragonal distortion alone, which drives the transition.

The relationship between the new magnetic ordering and potential electronic instabilities, flat bands and Weyl nodes, can be examined via the band structure of the low temperature phase in Fig. 5. In order to provide a direct comparison to the band structure and Weyl nodes of the ferromagnetic phase in Fig. 3, we have unfolded the bands of the low temperature cell into a Brillouin zone corresponding to that of the low temperature cubic primitive cell. We see that, in the low temperature structure, the flat band and several of the Weyl nodes have disappeared. The DOS pseudogap can be seen in the relatively empty region of the band structure about 0.2 eV below the Fermi level. Despite the formation of the pseudogap, a few Weyl nodes remain at the calculated Fermi level. Part of the discrepancy between our simulation and the expectation for the stabilization of a pseudogap *at the Fermi level* likely results from electron deficiency in the real material. As early as Butters and Myers' first study, Mn_3ZnC was found to have varying composition and magnetic properties with nominal Mn:Zn ratios greater than 3.[18] The Mn:Zn ratio of our best sample, measured by wavelength-dispersive X-ray fluorescence, was close to 3.76, which, in a rigid band approximation, would result in a deficiency of 0.8 electrons per primitive cubic cell and a Fermi level near the exact center of the pseudogap. We expect that the true

Mn:Zn ratio in our samples lies somewhere between the idealized value of 3.00 and the measured value of 3.76; while samples of this material appear pure in laboratory X-ray diffraction, synchrotron X-ray diffraction suggests that small nonmagnetic impurities of carbides Mn_5C_2 and Mn_7C_3 as well as MnO (which orders antiferromagnetically, but far lower in temperature than the transitions discussed here) may be present in addition to the majority Mn_3ZnC phase.[57]

Motivated by interest in these electronic structure changes associated with magnetostructurally coupled transitions, we performed experimental magnetoentropic characterization of both the high and low temperature transitions. Figure 6(a) presents magnetization data measured across the paramagnetic to ferromagnetic transition, which takes place near 420 K in our sample. While magnetization has been measured in older studies, to the best of our knowledge, no studies of the sharp, low field magnetization curves for either of the two magnetic transitions have been previously reported. Figure 6(b) shows the partial derivative, $\partial M/\partial T$, of these magnetization curves, displaying a large transition peak at low fields that reduces in magnitude and broadens as the field is increased. Figure 6(c) shows the magnetic entropy change, ΔS_M, across the transition. The magnitude of ΔS_M is a direct probe of the magnetostructural coupling strength in this compound.[58] The peak ΔS_M value is significant but not anomalous, suggesting medium magnetostructural coupling strength in this compound. Negative ΔS_M transitions are typical of the magnetocaloric effect seen in paramagnetic to ferromagnetic transitions in many magnetic materials. Characterization of the antiferromagnetic ordering transition in (d)–(f) is consistent with this finding. This transition is qualitatively similar in that it is sharp for low applied field, broad at high field, and has ΔS_M values with approximately the same magnitude of ≈0.1 J kg^{-1} K^{-1}. The positive sign of ΔS_M is typical of the inverse magnetocaloric effect seen at many antiferromagnetic ordering transitions.

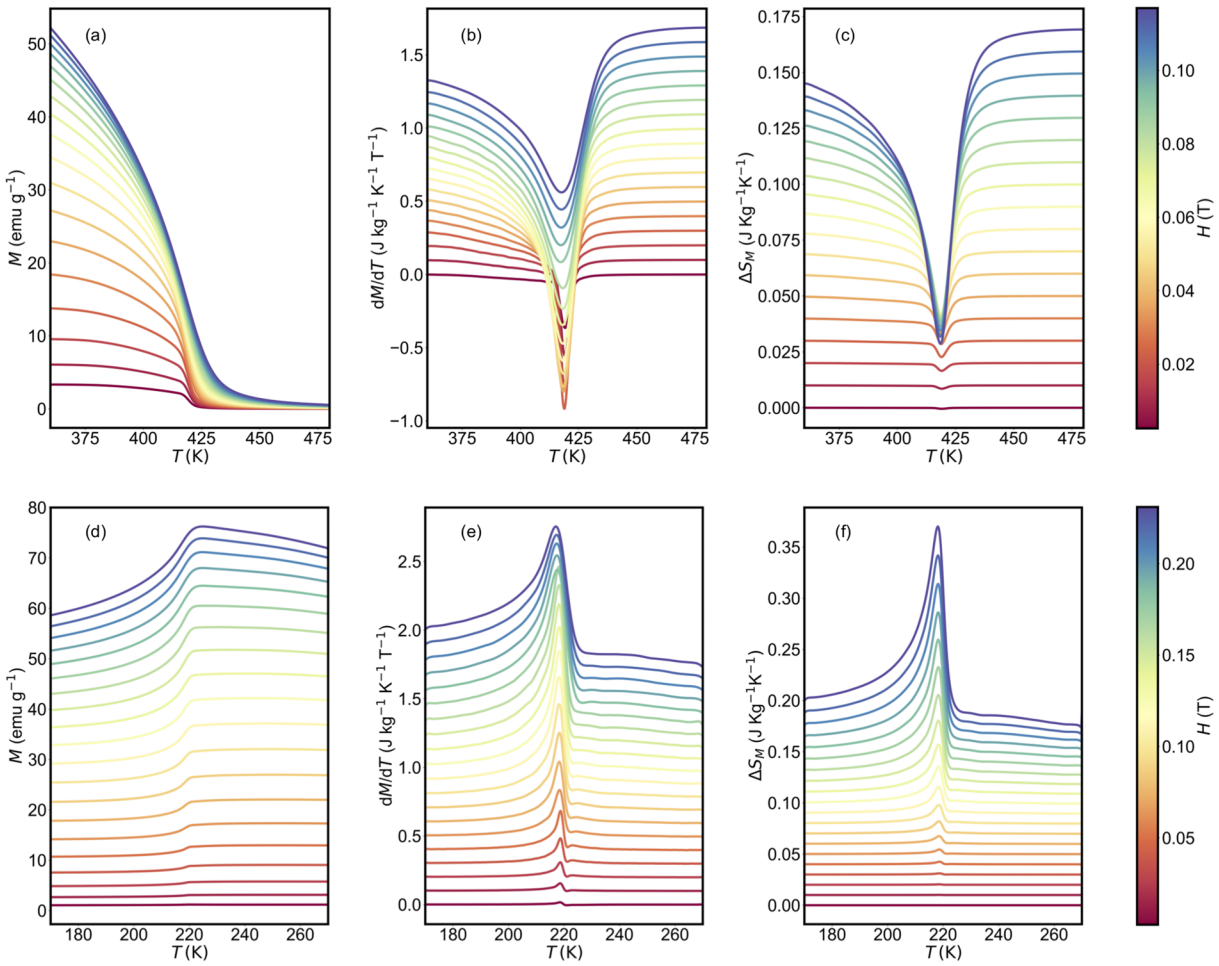

FIG. 6. Magnetoentropic mapping of the PM-FM and FM-NCL transitions. (a) Line plots of the magnetization, (b) magnetization derivative ($\partial M/\partial T$), and (c) magnetic entropy change (ΔS_M) taken under varying magnetic field are shown across the paramagnetic to ferromagnetic transition that occurs at approximately 420 K in our sample. (d)–(f) provide similar plots for the FM-NCL transition (≈219 K). Lines in [(b) and (e)] and [(c) and (f)] are offset by 0.1 and 0.01 units, respectively, for visual clarity.

IV. CONCLUSIONS

We have shown electronic structure simulations predicting that the room temperature phase of Mn_3ZnC is an exotic Weyl nodal line semimetal with nodal loops, isolated Weyl nodes, and drumhead surface states. The magnetic and electronic characterizations of the two transitions in this material that create and destroy this phase, meanwhile, appear relatively conventional. The upper transition can be explained by the reduction of near-Fermi level antibonding states and strengthening of Mn-Zn bonding, while the lower transition can be explained by the need to break symmetry and open a gap by expanding the unit cell to allow for antiferromagnetic ordering. An electronic Peierls distortion through antiferromagnetic ordering can allow for spin population energy shifts and the formation of a pseudogap that remove flatbands and Weyl nodes near the Fermi level. Despite the significant pseudogap, we found that a limited number of Weyl nodes still persist near the Fermi level in the low-temperature structure. However, even a small electron deficiency, expected based on the tendency toward Zn deficiency in experimental work, moves the Fermi level into the pseudogap of the low temperature structure.

There is interest at present in the Peierls-like structural distortions and phonon resonances associated with Weyl nodes.[59] The finding of Weyl nodal lines in Mn_3ZnC, a classic magnetic transition material, suggests that Weyl instability may play a role in a much wider range of magnetostructurally coupled materials. Many other magnetic materials that have a low temperature antiferromagnetic ordering likely transition through a semimetal state with near-Fermi level Weyl nodes. In fact, prototypical itinerant antiferromagnet chromium itself, the material for which the electronic Peierls instability concept was coined, hosts Fermi level Dirac crossings in non-spin polarized calculations, some of which are preserved in its transition to a low temperature antiferromagnetic ordering.[60] One major distinction between Mn_3ZnC and conventional antiferromagnetic materials is the reversed Peierls-like bonding structure with antibonding states below the Fermi level, nonbonding states at E_F, and bonding states just above. This reversed bonding structure is indicative of band inversion and could prove a useful hallmark in the search for topologically interesting magnets.

In addition to the bonding analysis we have presented to explain the structural transitions, important future work will focus on rigorously disentangling the relationship between Weyl nodes, flat bands, and phonon-mediated instabilities in Mn_3ZnC and related semimetals. There is incredible potential for nesting in the Fermi surface of Mn_3ZnC; the flat-bands alone, which perfectly bisect the Brillouin zone in k_x, k_y, k_z directions, provide maximal nesting at the calculated Fermi level in any supercell scheme as well as the tantalizing prospect of coupling flat-band-related correlation effects to Weyl physics. We urge caution. Just as flat band degeneracies in density functional theory are not a guarantee of interesting correlation effects in experiment, substantial evidence suggests that calculations of Fermi surface nesting are insufficient to prescriptively predict charge density waves, spin density waves, and other lattice incommensurate instabilities.[61] An important first step has been provided by a recent study on $(TaSe_4)_2I$, which relates the characteristic q-spacings of the Weyl nodes, peaks in the electronic susceptibility, and charge-density wave-modulation vectors observed in experimental X-ray measurements.[62]

Overall, our results suggest that compounds which display Weyl-like features in idealized high-symmetry structures may actually undergo transitions to more complex ground states than initially supposed.

SUPPLEMENTARY MATERIAL

See the supplementary material for additional experimental and computational details including discussion of the effects of spin-orbit coupling on the electronic structure.

ACKNOWLEDGMENTS

The work at UC Santa Barbara was supported by the National Science Foundation (NSF) through Grant No. DMR 1710638. L.M.S. was supported by the Princeton Center for Complex Materials, a Materials Research Science and Engineering Center (MRSEC) (Grant No. DMR 1420541). This research made use of shared facilities of the NSF MRSEC at UC Santa Barbara (Grant No. DMR 1720256). The UC Santa Barbara MRSEC is a member of the Materials Research Facilities Network (www.mrfn.org). We also acknowledge the use of the computing facilities of the Center for Scientific Computing at UC Santa Barbara supported by NSF Grant No. CNS 1725797 and NSF Grant No. DMR 1720256. Use of the Advanced Photon Source at Argonne National Laboratory was supported by the U.S. Department of Energy, Office of Science, Office of Basic Energy Sciences, under Contract No. DE-AC02-06CH11357. I.K.S. gratefully acknowledges support from the IRES: Cooperative for Advanced Materials in Energy-Related Applications (Grant No. NSF-OISE 1827034) and from AoA Materials Science, Chalmers University of Technology. S.M.L.T. was supported by the National Science Foundation Graduate Research Fellowship Program under Grant No. DGE-1650114. Any opinions, findings, and conclusions or recommendations expressed in this material are those of the authors and do not necessarily reflect the views of the National Science Foundation.

REFERENCES

[1] M. W. Barsoum, Prog. Solid State Chem. **28**, 201 (2000).
[2] Y. Kimura, Y. Mishima, and C. Liu, Intermetallics **9**, 1069 (2001).
[3] Y. Wen, C. Wang, Y. Sun, M. Nie, L. Fang, and Y. Tian, Solid State Commun. **149**, 1519 (2009).
[4] T. Hamada and K. Takenaka, J. Appl. Phys. **109**, 07E309 (2011).
[5] K. Kamishima, T. Goto, H. Nakagawa, N. Miura, M. Ohashi, N. Mori, T. Sasaki, and T. Kanomata, Phys. Rev. B **63**, 024426 (2000).
[6] T. He, Q. Huang, A. P. Ramirez, Y. Wang, K. A. Regan, N. Rogado, M. A. Hayward, M. K. Haas, J. S. Slusky, K. Inumara, H. W. Zandbergen, N. P. Ong, and R. J. Cava, Nature **411**, 54 (2001).
[7] S. Mollah, J. Phys.: Condens. Matter **16**, R1237 (2004).
[8] T. Kariyado and M. Ogata, J. Phys. Soc. Jpn. **80**, 083704 (2011).
[9] T. Kariyado and M. Ogata, J. Phys. Soc. Jpn. **81**, 064701 (2012).
[10] A. H. Castro Neto, F. Guinea, N. M. R. Peres, K. S. Novoselov, and A. K. Geim, Rev. Mod. Phys. **81**, 109 (2009).
[11] B.-J. Yang and N. Nagaosa, Nat. Commun. **5**, 4898 (2014).
[12] W. F. Goh and W. E. Pickett, Phys. Rev. B **97**, 035202 (2018).
[13] T. H. Hsieh, J. Liu, and L. Fu, Phys. Rev. B **90**, 081112 (2014).
[14] S. Suetsugu, K. Hayama, A. W. Rost, J. Nuss, C. Mühle, J. Kim, K. Kitagawa, and H. Takagi, Phys. Rev. B **98**, 115203 (2018).

[15]M. Oudah, A. Ikeda, J. N. Hausmann, S. Yonezawa, T. Fukumoto, S. Kobayashi, M. Sato, and Y. Maeno, Nat. Commun. **7**, 13617 (2016).
[16]R. Yu, H. Weng, Z. Fang, X. Dai, and X. Hu, Phys. Rev. Lett. **115**, 036807 (2015).
[17]Y.-H. Chan, C.-K. Chiu, M. Y. Chou, and A. P. Schnyder, Phys. Rev. B **93**, 205132 (2016).
[18]R. G. Butters and H. P. Myers, Philos. Mag. **46**, 132 (1955).
[19]B. N. Brockhouse and H. P. Myers, Can. J. Phys. **35**, 313 (1957).
[20]M. L. Swanson and S. A. Friedberg, Can. J. Phys. **39**, 1429 (1961).
[21]D. Fruchart and F. Bertaut, J. Phys. Soc. Jpn. **44**, 781 (1978).
[22]T. Kaneko, T. Kanomata, and K. Shirakawa, J. Phys. Soc. Jpn. **56**, 4047 (1987).
[23]D. Fruchart, E. Bertaut, B. L. Clerc, L. D. Khöi, P. Veillet, G. Lorthioir, E. Fruchart, and R. Fruchart, J. Solid State Chem. **8**, 182 (1973).
[24]T. Kaneko, T. Kanomata, S. Miura, G. Kido, and Y. Nakagawa, J. Magn. Magn. Mater. **70**, 261 (1987).
[25]J. P. Jardin and J. Labbé, J. Phys. **36**, 1317 (1975).
[26]K. Motizuki and H. Nagai, J. Phys. C: Solid State Phys. **21**, 5251 (1988).
[27]V. N. Antonov, B. N. Harmon, A. N. Yaresko, and A. P. Shpak, Phys. Rev. B **75**, 165114 (2007).
[28]D. Gosálbez-Martínez, I. Souza, and D. Vanderbilt, Phys. Rev. B **92**, 085138 (2015).
[29]I. Belopolski, K. Manna, D. S. Sanchez, G. Chang, B. Ernst, J. Yin, S. S. Zhang, T. Cochran, N. Shumiya, H. Zheng, B. Singh, G. Bian, D. Multer, M. Litskevich, X. Zhou, S.-M. Huang, B. Wang, T.-R. Chang, S.-Y. Xu, A. Bansil, C. Felser, H. Lin, and M. Z. Hasan, Science **365**, 1278 (2019).
[30]G. Kresse and J. Hafner, Phys. Rev. B **49**, 14251 (1994).
[31]G. Kresse and J. Furthmüller, Phys. Rev. B **54**, 11169 (1996).
[32]G. Kresse and J. Furthmüller, Comput. Mater. Sci. **6**, 15 (1996).
[33]P. Blaha, K. Schwarz, G. Madsen, D. Kvasnicka, and J. Luitz, *WIEN2K: An Augmented Plane Wave and Local Orbitals Program for Calculating Crystal Properties* (Karlheinz Schwarz, 2001).
[34]J. P. Perdew, K. Burke, and M. Ernzerhof, Phys. Rev. Lett. **77**, 3865 (1996).
[35]P. E. Blöchl, Phys. Rev. B **50**, 17953 (1994).
[36]G. Kresse and D. Joubert, Phys. Rev. B **59**, 1758 (1999).
[37]K. Schwarz, P. Blaha, and G. Madsen, Comput. Phys. Commun. **147**, 71 (2002).
[38]P. E. Blöchl, O. Jepsen, and O. K. Andersen, Phys. Rev. B **49**, 16223 (1994).
[39]A. A. Mostofi, J. R. Yates, G. Pizzi, Y.-S. Lee, I. Souza, D. Vanderbilt, and N. Marzari, Comput. Phys. Commun. **185**, 2309 (2014).
[40]Q.-S. Wu, S.-N. Zhang, H.-F. Song, M. Troyer, and A. A. Soluyanov, Comput. Phys. Commun. **224**, 405 (2018).
[41]M. P. L. Sancho, J. M. L. Sancho, J. M. L. Sancho, and J. Rubio, J. Phys. F: Met. Phys. **15**, 851 (1985).
[42]P. V. C. Medeiros, S. Stafström, and J. Björk, Phys. Rev. B **89**, 041407 (2014).
[43]P. V. C. Medeiros, S. S. Tsirkin, S. Stafström, and J. Björk, Phys. Rev. B **91**, 041116 (2015).
[44]R. Dronskowski and P. E. Bloechl, J. Phys. Chem. **97**, 8617 (1993).
[45]V. L. Deringer, A. L. Tchougréeff, and R. Dronskowski, J. Phys. Chem. A **115**, 5461 (2011).
[46]S. Maintz, V. L. Deringer, A. L. Tchougréeff, and R. Dronskowski, J. Comput. Chem. **34**, 2557 (2013).
[47]S. Maintz, V. L. Deringer, A. L. Tchougréeff, and R. Dronskowski, J. Comput. Chem. **37**, 1030 (2016).
[48]K. Momma and F. Izumi, J. Appl. Crystallogr. **44**, 1272 (2011).
[49]J. D. Bocarsly, R. F. Need, R. Seshadri, and S. D. Wilson, Phys. Rev. B **97**, 100404 (2018).
[50]R. Dronskowski, K. Korczak, H. Lueken, and W. Jung, Angew. Chem., Int. Ed. **41**, 2528 (2002).
[51]R. Hoffmann, Angew. Chem., Int. Ed. **26**, 846 (1987).
[52]J. Wang, Y. Liu, K.-H. Jin, X. Sui, L. Zhang, W. Duan, F. Liu, and B. Huang, Phys. Rev. B **98**, 201112 (2018).
[53]S. M. L. Teicher, L. K. Lamontagne, L. M. Schoop, and R. Seshadri, Phys. Rev. B **99**, 195148 (2019).
[54]Z. Wang, M. G. Vergniory, S. Kushwaha, M. Hirschberger, E. V. Chulkov, A. Ernst, N. P. Ong, R. J. Cava, and B. A. Bernevig, Phys. Rev. Lett. **117**, 236401 (2016).
[55]D. Vanderbilt, *Berry Phases in Electronic Structure Theory* (Cambridge University Press, 2018).
[56]N. P. Armitage, E. J. Mele, and A. Vishwanath, Rev. Mod. Phys. **90**, 015001 (2018).
[57]P. Karen, H. Fjellvåg, A. Kjekshus, and A. F. Andresen, Acta Chem. Scand. **45**, 549 (1991).
[58]V. Franco, J. Blázquez, B. Ingale, and A. Conde, Annu. Rev. Mater. Res. **42**, 305 (2012).
[59]J.-H. Park, S. H. Lee, C. H. Kim, H. Jin, and B.-J. Yang, Phys. Rev. B **99**, 195107 (2019).
[60]A. Decker, G. A. Landrum, and R. Dronskowski, Z. Anorg. Allg. Chem. **628**, 303 (2002).
[61]M. D. Johannes and I. I. Mazin, Phys. Rev. B **77**, 165135 (2008).
[62]W. Shi, B. J. Wieder, H. L. Meyerheim, Y. Sun, Y. Zhang, Y. Li, L. Shen, Y. Qi, L. Yang, J. Jena, P. Werner, K. Koepernik, S. Parkin, Y. Chen, C. Felser, B. A. Bernevig, and Z. Wang, e-print arXiv:1909.04037 (2019).